Modeling of Inclusion Growth and Dissolution in the Weld Pool

T. HONG, T. DEBROY, S.S. BABU, and S.A. DAVID

The composition, size distribution, and number density of oxide inclusions in weld metal are critical factors in determining weldment properties. A computational model has been developed to understand these factors, considering fluid flow and the temperature field in the weld pool during submerged arc (SA) welding of low-alloy steels. The equations of conservation of mass, momentum, and energy are solved in three dimensions to calculate the velocity and temperature fields in the weld pool. The loci and corresponding thermal cycles of thousands of oxide inclusions are numerically calculated in the weld pool. The inclusions undergo considerable recirculatory motion and experience strong temperature gyrations. The temperature-time history and the computed time-temperature-transformation (TTT) behavior of inclusions were then used to understand the growth and dissolution of oxide inclusions in the weld pool. The statistically meaningful characteristics of inclusion behavior in the weld pool, such as the residence time, number of temperature peaks, *etc.*, were calculated for several thousand inclusions. The calculated trends agree with experimental observations and indicate that the inclusion formation can be described by combining thermodynamics and kinetics with the fundamentals of transport phenomena.

I. INTRODUCTION

THE integrity of welded joints depends on the geometry, composition, macrostructure, and microstructure of the weldments. In low-alloy steel welds, the amounts of various ferrite morphologies, such as allotriomorphic ferrite, acicular ferrite, bainite, and martensite play a critical role in the final properties. Moreover, oxide inclusions in the weld also affect the weld properties by affecting microstructural development. Critical to the development of the weld-metal microstructure are the composition, morphology, and distribution of inclusions.[1] Oxide inclusions are most common in steel weldments. In general, the presence of inclusions is detrimental to weld properties. However, under a given set of conditions, in low-alloy steel welds, certain oxide inclusions promote the formation of an acicular ferrite phase, which improves toughness.[2–7] On the other hand, the presence of a very high volume fraction of inclusions may initiate premature ductile fracture.

Although the importance of inclusions in affecting weld-metal properties has been recognized for a long time, it is only in recent years that systematic studies of inclusions in weld metals have begun. The oxide and other inclusions are affected by the concentrations of oxygen and alloying elements in the weld metal. Frost and Olson[2] showed that microsegregation during weld-pool solidification leads to significant enrichment of oxygen and deoxidants in the interdendritic liquid. These authors considered the effect of this enrichment on the sequence of oxide formations during the final stages of solidification. Barbaro *et al.*[3] concluded that oxide inclusions are likely to be effective in controlling acicular ferrite formation and grain coarsening, even in the heat-affected zone (HAZ), as compared to carbide and nitride precipitates. The oxide inclusions containing γ-Al_2O_3, titanium oxide (Ti_xO_y), and galaxite ($MnO{\cdot}Al_2O_3$), with diameters larger than 0.4 μm, are often found to be effective nucleation sites for acicular ferrite.[4]

Kluken and Grong studied mechanisms of inclusion formation in Al-Ti-Si-Mn steel weld metals[4] and precipitate stability in weld metals.[6] They calculated the volume fraction, size, and chemical composition of inclusions from weld-metal chemistry. They determined the volume fraction of inclusions from an empirical relation involving both oxygen and sulfur concentrations. They modeled the chemical composition of inclusions in low-alloy steel welds as a function of weld-metal chemistry, with stoichiometric relations and a fixed oxidation sequence based on the standard free energy of oxide formation. Kluken and Grong also showed that welding parameters have a significant effect on the size distribution of oxide inclusions, and they related the same to Ostwald ripening mechanisms. However, they ignored the effects of weld-metal composition and cooling rate. Hsieh *et al.*[8] predicted sequential inclusion formation in low-alloy steel welds, considering equilibrium thermodynamics. This method considered the weld-metal composition but ignored the temperature histories of inclusions. The temperature histories are important for the calculation of inclusion growth and dissolution rates.

The rate of precipitation of the oxide inclusion from a supersaturated liquid can be determined from the nucleation and diffusion rates of the elements to the reaction interface. Babu *et al.*[9,10] have shown that the number density of inclusions can be calculated from the nucleation rate of the first-forming oxide. Therefore, by relating the time spent in the temperature range of the first-forming oxide, the effect of the weld-metal cooling rate on the inclusion number density can be described. However, this method considered monotonous cooling of the liquid steel region, and it is well known that the inclusions may experience thermal excursions because of fluid flow conditions.

T. HONG, Graduate Student, and T. DEBROY, Professor, are with the Department of Materials Science and Engineering, Pennsylvania State University, University Park, PA 16802. S.S. BABU, Development Staff, and S.A. DAVID, Corporate Fellow and Group Leader, are with the Metals and Ceramics Division, Oak Ridge National Laboratory, Oak Ridge, TN 37831-6095.

Manuscript submitted October 22, 1998.

Inside the weld pool, molten liquid undergoes vigorous circulation resulting from buoyancy, surface tension, and, when electric current is used, electromagnetic forces.[11,12] As an oxide inclusion is transported by convective currents in the weld pool, it will grow or dissolve along its path, depending on the temperature it experiences. At any given instant, its velocity and temperature depend on the velocity and temperature fields prevailing in the location. Understanding the thermal histories and corresponding growth/dissolution of a large number of inclusions is a prerequisite for the understanding of the size distribution, composition, and other properties of inclusions in the weld pool, for a given welding condition.

To address the proceeding phenomena, Hong *et al.*[11] developed a technique to calculate the size distribution of inclusions, considering fluid flow as well as the thermodynamics and kinetics of inclusion growth and dissolution. In this method, the temperature histories and loci of a large amount of inclusions were calculated under different welding parameters to study the effect of welding parameters on inclusion size distribution. However, very little effort has been made to extend these new capabilities to study inclusion formation over a wide range of welding processes such as submerged arc (SA), gas metal arc, shielded metal arc, and laser welding. Such an approach is preferred over the conventional analytical equation of heat transfer in order to understand the details of the inclusion formation. For example, in the recent past, calculations of fluid flow and heat transfer[13,14] have provided significant insights into the weld-pool formation, which could not be achieved otherwise.

Therefore, in this article, the temperature and velocity fields of the weld pool are used to understand inclusion growth in the SA welding process. The path, temperature history, velocities, and kinetics of oxygen diffusion–controlled growth and the dissolution of thousands of Al_2O_3 inclusions are examined computationally, considering the fact that they experience temperature excursions in the weld pool. The calculated number density result was modified by a separated collision model.[15,16] The calculated results were compared to the experimentally determined results.[9] In all experiments, bead-on-plate welds were made on a 20-mm-thick plate. In the calculation, the composition of the weld pool was taken to be the same as the chemistry of the base plate. The effects of flux and filter compositions were not considered, since we are dealing with inclusion formation for a given oxygen level. The welding parameters and some material data used are shown in Table I. The composition of the low-alloy steel is Fe-0.066C-0.82Si-1.66Mn-0.03Ni-0.05Cr-0.025Ti-0.026Al-0.007N-0.0840.

Table I. Data Used for the Calculation of Temperature and Velocity Fields

Parameters	Values
Welding process	submerged arc welding
Welding voltage	29 V
Welding current	580 A
Interpass temperature	523 K
Welding speed	9.2 mm/s
Density	7200 kg/m^3
Solidus temperature	1745 K
Liquidus temperature	1780 K
Viscosity of liquid	0.024 kg/m s
Thermal conductivity of solid	20.9 W/m K
Thermal conductivity of liquid	334.7 W/m K
Enthalpy of solid at melt point*	1.05×10^6 J/kg
Enthalpy of liquid at melt point*	1.32×10^6 J/kg
Diffusion coefficient of oxygen in steel	1×10^{-8} m^2/s
Specific heat of solid	703 J/kg K
Specific heat of liquid	808 J/kg K

*The reference point of these enthalpy values is at 298 K.

II. CALCULATION PROCEDURE

A. *Temperature and Velocity Fields in the Weld Pool*

The temperature and velocity fields and the shape and size of the weld pool are calculated through the solution of the equations of conservation of mass, momentum, and energy in three dimensions. Using the finite-difference method, the coordinate system of the grid was fixed to the moving heat source. A heat flux with Gaussian distribution was considered in this model. The governing equations are modified according to the fixed grid system. The basic features of the calculations are as follows.[12,17]

(1) A control-volume technique and the SIMPLER algorithm, described by Patankar,[17] were implemented for the discretization of the governing equations and were used to solve the governing equations.
(2) The net velocity in the computational domain is subdivided into two parts: convective velocity as the primary unknown velocity, and welding velocity.
(3) The source terms in the momentum and energy equations are modified for a fixed-grid system using the upwind scheme.
(4) The enthalpy-porosity technique, which divides the total enthalpy into a sum of sensible heat and latent heat content, is applied to the heat-transfer model and phase-change calculation.
(5) The heat input from droplets was considered as one part of the source term.

The model has been verified by comparing many experimental measurements of the weld-pool geometry at several selected locations in the weldments to the corresponding calculated results. Good agreement was achieved between the experimental and the predicted values of the weld-pool width and depth.

The welding variables and data used for these calculations are presented in Table I. A $50 \times 28 \times 26$ nonuniform computational mesh, which is finer near the heat source, was used to obtain maximum resolution. The details of the calculation procedure have been presented in a previous article.[12]

B. *Inclusion Formation and Growth Model*

The following assumptions were made to simplify the calculations

(1) Only Al_2O_3 is considered in this work.
(2) The chemical composition of the weld pool is assumed to be uniform.

(3) At an instant, Al_2O_3 nuclei are assumed to exist in all the locations at the molten liquid steel.
(4) The growth and dissolution rates of the inclusion are determined by the diffusion rate of oxygen alone.
(5) Inclusions are independent of each other. Possible overlapping of concentration fields is not considered. No collision and coalescence of inclusions was considered during the formation and dissolution. However, the collision and coalescence were considered to modify the final inclusion size distribution. The collision and coalescence model is explained in the Appendix.
(6) Local equilibrium was assumed at the interface between the inclusion and the liquid metal.
(7) A constant diffusivity of oxygen was assumed.

The driving force for an oxide formation can be indicated as the Gibbs free-energy change (ΔG) associated with the formation reaction on the interface between an oxide inclusion and liquid steel,

$$\Delta G = \Delta G^0 + \mathrm{R}T\ln\left(\frac{a_{M_xO_y}}{a_M^x a_O^y}\right), \text{for } xM + y\,\mathrm{O} = M_x\mathrm{O}_y \quad [1]$$

where ΔG^0 is the standard free energy for this reaction, T is the temperature, and a_M, a_O, and $a_{M_xO_y}$ are the activities of the dissolved metal, oxygen, and metal oxide, respectively. The free energy of formation of various oxides is highly sensitive to the concentration term, especially at low concentrations. Hence, the stability of various oxides in equilibrium with liquid steel will be a function of composition. Considering the stoichiometry and the mass balance before and after the reaction, one can write

$$[\text{pct } M] = [\text{pct } M_{\text{orig}}] - \frac{xM_M}{yM_O}([\text{pct O}_{\text{orig}}] - [\text{pct O}]) \quad [2]$$

where [pct M] and [pct O] are the equilibrium concentrations of metal and oxygen at the interface in weight percentage, [pct M_{orig}] and [pct O_{orig}] are the original concentrations of metal and oxygen in bulk in weight percentage, and M_M and M_O are the atomic weights of metal and oxygen. From Eqs. [1] and [2], we can solve the equilibrium concentrations of oxygen and metal at the interface of inclusion and liquid steel.

In some cases, such as ordinary ladle-refined steel, homogeneous nucleation of oxide inclusions may occur in certain regions of the melt where the supersaturation is sufficiently high. In this calculation, we calculated the nucleation rate of inclusions (I_v), considering homogeneous nucleation for simplicity:

$$I_v = A\exp\left(\frac{-\Delta G^*_{\text{hom}}}{\mathrm{k}_0 T}\right) = A\exp\left(-\frac{16\pi\sigma^3 V_m^2}{3\mathrm{k}_0 T\Delta G^2}\right) \quad [3]$$

where ΔG^*_{hom} is the activation energy for the formation of the oxide nucleus for homogeneous nucleation, ΔG can be calculated from Eq. [1], A is a constant equal to 10^{33} m^{-3} s^{-1}, V_m is the molar volume of the oxide inclusion, σ is the interfacial energy of the inclusion, equal to 0.5 J m^{-2}, and k_0 is the Boltzmann's constant. The interaction parameters and the standard free energies of formation of oxides can be obtained from References 9 and 18.

The growth of inclusions was assumed to be controlled by diffusion of oxygen and of the deoxidizing alloy element in the weld pool toward the oxide nuclei. The inclusions are assumed to be spherical particles. The approach for diffusion-controlled growth of precipitates in solid solutions, described by Zener,[19] can be applied to inclusion growth in liquid steel.

$$r = \sqrt{-\mathrm{k}D_O t} = \alpha_3^* \sqrt{t} \quad [4]$$

where D_O is the diffusion coefficient of oxygen in the alloy, r is the radius of the inclusion, t is the growth time after nucleation, and α_3^* is the parabolic thickening-rate constant, given by

$$\alpha_3^* = \sqrt{-D_O\mathrm{k}} \quad [5]$$

with the condition $|\mathrm{k}| \ll 1$. The constant k is defined as

$$\mathrm{k} = 2(c_O^{il} - c_O^l)/(c_O^i - c_O^{il}) \quad [6]$$

where c_O^l is the nominal concentration of oxygen far away from the inclusion/liquid interface, and c_O^i and c_O^{il} are the concentrations of oxygen in the inclusion and in the inclusion/liquid interface, respectively. These concentrations can be obtained from the definitions of activity and from the solution of Eqs. [1] and [2].

Combining these concentrations with both the nucleation rate and the growth rate of oxide inclusions, an overall kinetic approach is applied. This approach is discussed in detail by Christian[20] for precipitation from a supersaturated solution involving long-range diffusion and precipitation. The extent of transformation (ζ) as a function of time is given by

$$\zeta = 1 - \exp\left(-((c_M^i - c_M^{il})/(c_M^l - c_M^{il}))I_v(8\pi/15)(\alpha_3^*)^3 t^{5/2}\right) \quad [7]$$

where c_M^l is the nominal concentration of the metal element far away from the inclusion/liquid interface, and c_M^i and c_M^{il} are the concentrations of metal in the inclusion and in the inclusion/liquid interface, respectively. For a given steel composition, the time-temperature-transformation (TTT) diagram of various oxide inclusions can be calculated using Eqs. [1] through [7]. We have used these equations in a previous article to calculate the TTT diagram for inclusion formation.[9] Here, we extend the calculations by following the loci and temperature excursions of a large number of growing inclusions to understand their growth. The moving velocity of the interface between the inclusion and liquid metal (v), which is the rate of the increase in inclusion radius, can be written as

$$v = \frac{dr}{dt} = \frac{d\alpha_3^*}{dt}\sqrt{t} + \frac{\alpha_3^*}{2\sqrt{t}} \quad [8]$$

The concentration of oxygen at the interface is a function of temperature and alloy composition. As a result, for a given composition, the constant and the thickening rate depend on temperature. The relationship between thickening rate and temperature is calculated from Eqs. [1], [2], [6], and [7]. It was found from the calculated results that α_3^* changed by less than 10 pct when the temperature changes from 1700 to 2200 K. This result is also caused by the constant diffusivity we assumed. Therefore, its change with temperature (and time) may be neglected. Also, because we assume uniform chemical composition and constant diffusivity, the change in α_3^* becomes very small. From Eq. [8], the change in the radius (Δr) during a small time step (Δt) can be written as

$$\Delta r = \frac{\alpha_3}{2\sqrt{t}}\,\Delta t \qquad [9]$$

For the dissolution of the inclusions, Whelan[21] considered a solution to the diffusion equation with a stationary-interface approximation. By considering the Laplace approximation for short times, a simple approximate solution was obtained:

$$\Delta r = -\frac{k}{2}\left(\frac{D_O}{r} + \sqrt{\frac{D_O}{\pi t}}\right)\Delta t \qquad [10]$$

where k is defined by Eq. [6], D_O is the oxygen diffusion coefficient in the bulk, Δr is the change of the inclusion radius, and Δt is the time-step. Because the inclusions move rapidly in the elevated-temperature regions, the concentration field near each inclusion is assumed to be constant during the dissolution of the oxide inclusion.

C. *Trajectories and Thermal Histories of Inclusions*

Calculation of the Al_2O_3 inclusion trajectory is actually an initial-value problem, which is solved by approximating the exact solution at a number of mesh points, starting from the initial point and moving forward. Because the inclusions can nucleate at any place in the weld pool where the temperature is below 2200 K, all the grid points in the liquid region of the weld pool were considered to be the initial points. With this notion, the thermal history and growth/dissolution behavior of each point was calculated one by one. The derivative of the inclusion path with respect to time depends on the local fluid velocity. Therefore, the fluid-flow velocity at the current location of the inclusion had to be determined by interpolation from adjacent points. A "predictor-corrector algorithm" is used to solve the initial-value problem. The Adams–Bashforth[22] formula is used to predict the inclusion location at the next time step, and then an Adams–Moulton[22] formula is used to correct the predicted value. The four-step Adams–Bashforth formula is used to predict the approximate solution in the inclusion tracking calculation,

$$\mathbf{r}(t_{i+1}) = \mathbf{r}(t_i) + \frac{h_i}{24}\left(55\,\mathbf{v}(t_i, \mathbf{r}_i) - 59\,\mathbf{v}(t_{i-1}, \mathbf{r}_{i-1}) + 37\,\mathbf{v}(t_{i-2}, \mathbf{r}_{i-2}) - 9\,\mathbf{v}(t_{i-3}, \mathbf{r}_{i-3})\right) \qquad [11]$$

where t_i is the time at the ith time step, r_i is the location of the inclusion at the ith time step, $\mathbf{v}(t_i, \mathbf{r}_i)$ is the velocity of the inclusion in the ith time-step and at the $\mathbf{r}_i$ location, and h_i is the time gap in the ith time-step. Then, using the three-step Adams–Moulton algorithm to correct the predicted value with $r(t_{i+1})$, we get, from Eq. [11],

$$\mathbf{r}(t_{i+1}) = \mathbf{r}(t_i) + \frac{h_i}{24}\left(9\,\mathbf{v}(t_{i+1}, \mathbf{r}_{i+1}) + 19\,\mathbf{v}(t_i, \mathbf{r}_i) - 5\,\mathbf{v}(t_{i-1}, \mathbf{r}_{i-1}) + \mathbf{v}(t_{i-2}, \mathbf{r}_{i-2})\right) \qquad [12]$$

The time gap of each time-step is determined in a adaptive way when the global error is found to be too big or too small.

D. *Calculation of Number Density*

The nucleation rates in different grids of the weld pool were taken into account to estimate the number density.

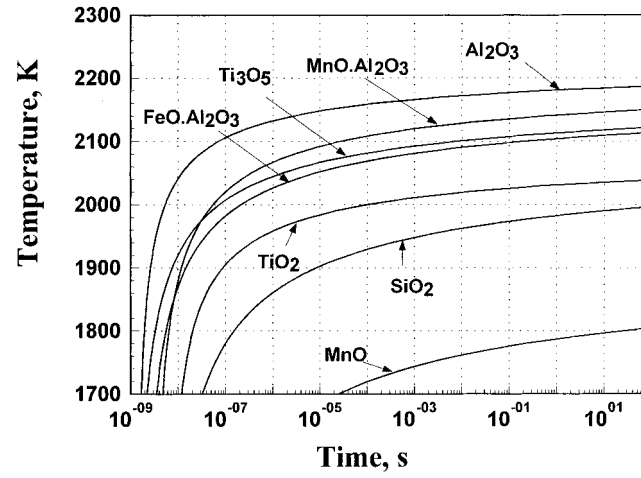

Fig. 1—TTT diagram of the formation of different kinds of oxide inclusion in low alloy steel ($\zeta = 0.1$ in Eq. [7]) in low alloy steel of the following composition: 0.066 pct C, 0.82 pct Si, 1.66 pct Mn, 0.03 pct Ni, 0.05 pct Cr, 0.025 pct Ti, 0.026 pct Al, 0.007 pct N, 0.084 pct O.

When the final size of an inclusion is obtained, we traced back to its original location and calculated the nucleation rate in this location at different temperatures. The product of the nucleation rate and the time spent by the inclusion at that instance would be used to determine the final number density. The final calculation of the inclusion number density can be explained by the following equation:

$$\text{number density of inclusion for specific size} = \sum_{i=1}^{n} I_\nu^{\text{oxide}} \times t \qquad [13]$$

where n is the number of inclusions with such a size, I_ν^{oxide} is the homogeneous nucleation rate as a function of temperature, and t is the residence time of the inclusions at that instance at that location in the weld pool. Note that it is an approximate calculation and does not consider all nucleation events, and that the final value is only an estimation of the number density. However, we can observe the trends for a given condition. Finally, the collision models developed by Iyengar and Philbrook[15] and by Lindborg and Torssell[16] were used to modify the calculated number-density result to account for the collision among inclusions. The details of the collision model are given in the Appendix.

III. RESULTS AND DISCUSSIONS

A. *TTT Diagrams for Inclusion Growth and Dissolution*

Figure 1 is the computed TTT diagram for a 1 pct completion of inclusion formation ($\zeta = 0.01$ in Eq. [7]), which describes the beginning of oxide inclusion formation. The plots show that the sequence of inclusion formation is Al_2O_3, $MnO \cdot Al_2O_3$, Ti_3O_5, $FeO \cdot Al_2O_3$, TiO_2, SiO_2, and MnO, which agrees with the results calculated in Reference 9. With thermodynamic calculation, Hsieh *et al.*[8] showed that Al_2O_3 is the most-stable oxide inclusion at high temperatures. The TTT diagram shows that no oxide inclusion will form above 2200 K. On the other hand, temperatures in the weld pool often reach levels near 2500 K. At these temperatures, oxide inclusions will dissolve. However, while cooling, the first

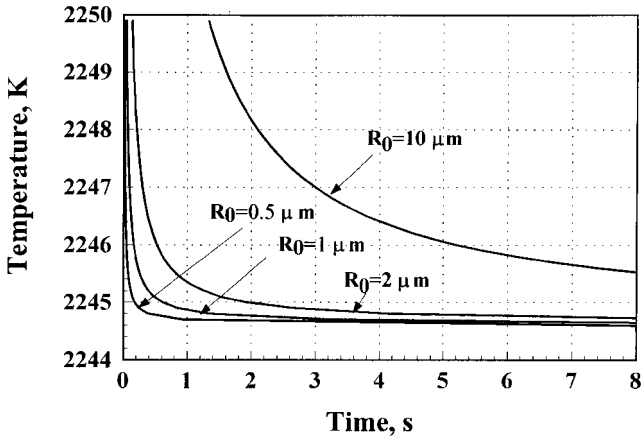

Fig. 2—Time-temperature diagram of the dissolution of Al_2O_3 inclusion (99 pct reduction in diameter) with different initial sizes.

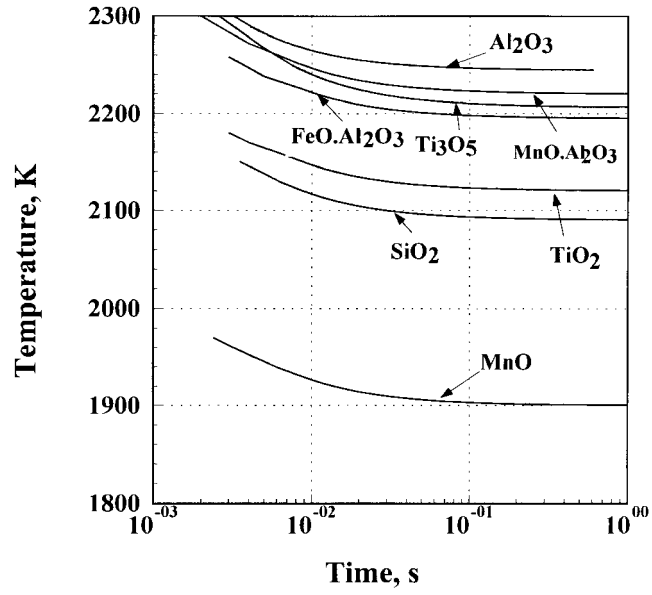

Fig. 3—Time-temperature diagram of the dissolution of different oxide inclusions (99 pct reduction in diameter) with the initial size of 1 μm.

oxide to form will be Al_2O_3. In this work, the reduction in oxygen and aluminum concentrations with the progress of inclusion growth was ignored. This assumes an infinite supply of [O] and [Al] to the growth of Al_2O_3. Therefore, the dissolution and growth of an Al_2O_3 inclusion, as a function of thermal cycle, was the only goal of this work.

Figure 2 is the temperature-time curve for the 99 pct dissolution of Al_2O_3 for different sizes. It is observed that Al_2O_3 inclusions will not dissolve below 2245 K. Moreover, the temperature change has a significant effect on the dissolution rate. For example, when the temperature is 2250 K, it takes only about one-tenth of the time required at 2245 K for complete dissolution. The size effect on the dissolution can also be observed from the graph. The bigger the inclusion, more difficult the completion of dissolution. It is observed from the graph that it will take more than 10 seconds to completely dissolve an inclusion of more than 10 μm in diameter. This means that if a large inclusion reaches the high-temperature region, it is unlikely to dissolve completely. The temperature-time curves of 99 pct dissolution of different kinds of inclusions are shown in Figure 3. It shows that Al_2O_3 is the most-stable oxide at high temperatures.

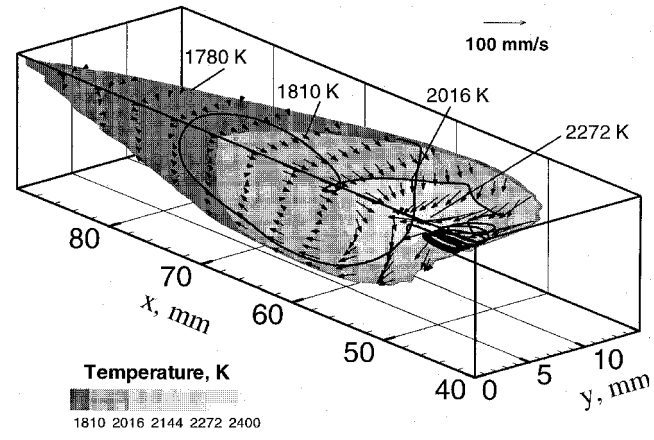

Fig. 4—Temperature and velocity fields considering turbulence flow in submerged arc welding and a typical inclusion loci in the weld pool. Welding parameters: welding current, 580 A; welding voltage, 29 V; interpass temperature, 523 K; and welding speed, 9.2 mm/s

B. *Calculated Weld-Pool Geometry*

The computed temperature field, presented in Figure 4, is typical of fusion welding. The figure shows higher temperature gradients ahead of the heat source than behind it. The calculated maximum cross-sectional area was compared to the experimental weld-pool geometry in Figure 5. The Marangoni force is a major driving force for the circulation of liquid metal in the weld pool. Since the spatial gradient of temperature determines the Marangoni stress, the velocity values ahead of the weld pool are higher than the velocity values behind the heat source. The resulting Marangoni stress leads to fluid convection in the weld pool. The velocities in the weld pool are away from the heat source toward the periphery of the weld pool. The calculated weld-pool depth and width were in good agreement with the corresponding experimental data (Figure 5). The calculated temperature and velocity fields provide the basis for understanding inclusion growth, considering their recirculatory motion in the weld pool and their temperature excursions.

C. *Inclusion Motion and Thermal Excursions in the Weld Pool*

To calculate the loci of the Al_2O_3 inclusions in the weld pool, the drag effect on the inclusion is not considered. This simplification is reasonable, because the main oxide inclusion, Al_2O_3, has a low density and its size is very small (<1 μm). The error in the streamlines resulting from this assumption was calculated to be negligible.[23] The thermal history and trajectories of thousands of Al_2O_3 inclusions in the weld pool were calculated using the aforementioned procedure. The selected initial locations of Al_2O_3 inclusions are distributed uniformly in the liquid region based on the computational grid point. The size of the liquid region

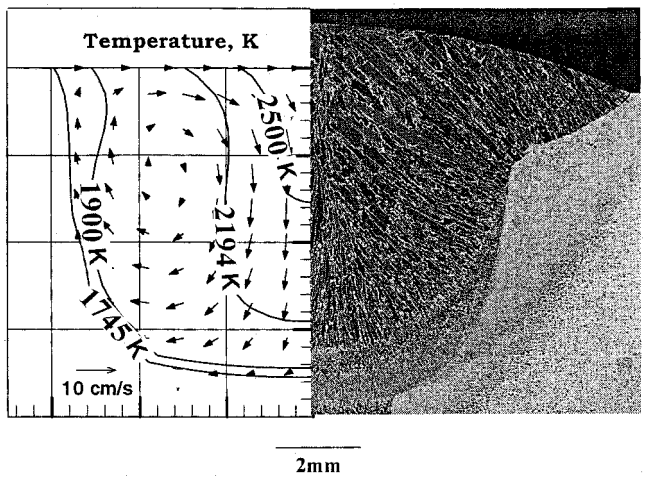

Fig. 5—Comparison of the calculated and experimental cross-sectional area of the submerged arc welding pool.

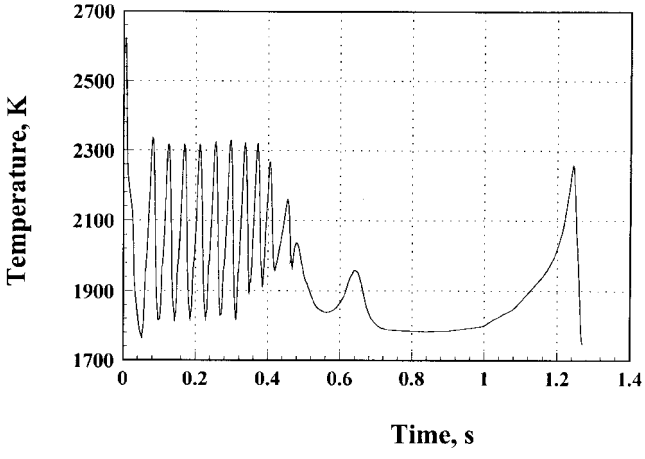

Fig. 6—Temperature-time curve along the inclusion loci shown in Fig. 4.

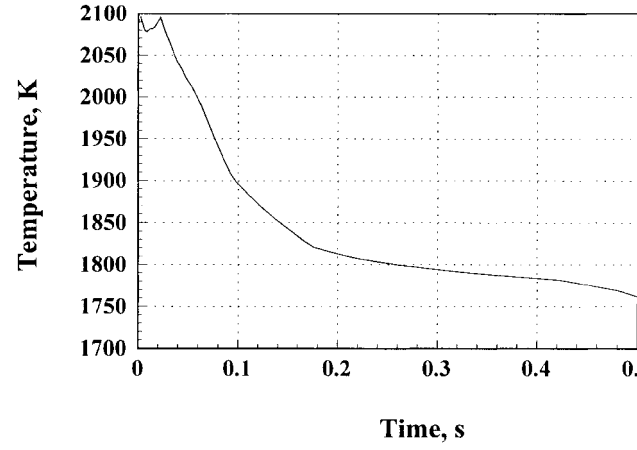

Fig. 7—Continuous cooling behavior experienced by an inclusion.

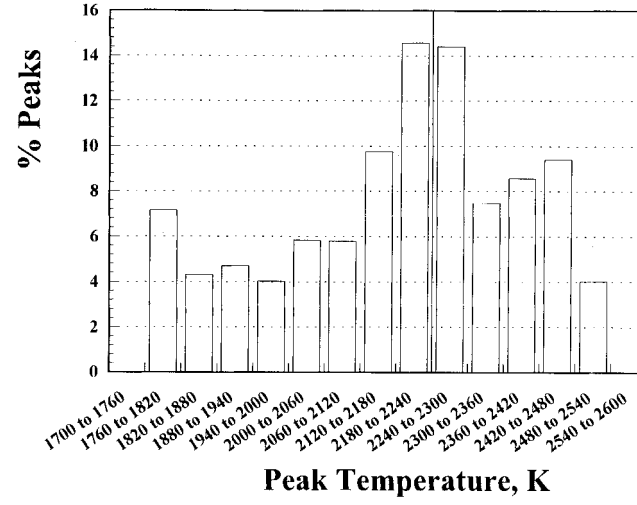

Fig. 8—Temperature peak distribution experienced by thousands of Al_2O_3 inclusions in the weld pool.

depended on the welding variables. Therefore, the number of initial locations of the inclusions also depended on the welding variables. A typical locus of an inclusion is also shown in Figure 4. The locus of the inclusion is shown by the thick solid line within the weld pool. It can be observed that the inclusion undergoes vigorous circulation in the weld pool. The corresponding temperature gyrations along the path of the inclusion are shown in Figure 6. In most cases, the thermal history of the inclusions had several characteristic peaks. However, Figure 7 shows a continuous cooling behavior experienced by a large proportion of the inclusions, without any temperature peak after they were nucleated. The nature of the temperature-time plot depends on the initial location of the inclusion. Generally, an inclusion with continuous cooling behavior has a bigger probability of nucleating in the region with small fluid-flow velocities, *i.e.*, near the fusion/HAZ boundary. The reason is that the inclusions in the outer part of the weld pool are likely to be lead to the solid region along the fluid-flow direction without any temperature gyration. The average residence time of this SA welding is about 0.58 seconds.

The peak temperature that the inclusions can attain has a wide distribution, from the melting point of 1750 K to the highest temperature of about 2550 K, as shown in Figure 8. In addition, we can estimate the average temperature (T_a) experienced by an inclusion using the following relation:

$$T_a = \frac{\sum_{i=1}^{n} T_i \Delta t_i}{\sum \Delta t_i} \qquad [14]$$

where T_i is the instantaneous temperature and Δt_i is the time-step. The calculated average temperature (2040 K) is lower than the mean temperature (2150 K) and in between the liquidus temperature (1750 K) and the maximum temperature (2550 K) in the weld pool. The reason for the lower-than-average temperature experienced by the inclusions can be understood from the consideration of the velocity and the temperature fields in the weld pool. The weld-pool temperatures are highest where the heat source impinges on the weld-pool surface. The liquid-metal velocities are also highest in this region. Because of the large velocities prevailing at the high-temperature regions of the pool, the inclusions spend shorter periods in the hot regions and a longer time in the relatively cold regions. As a result, the average temperatures are always lower than the average of the liquidus temperature and the peak temperature in the weld pool.

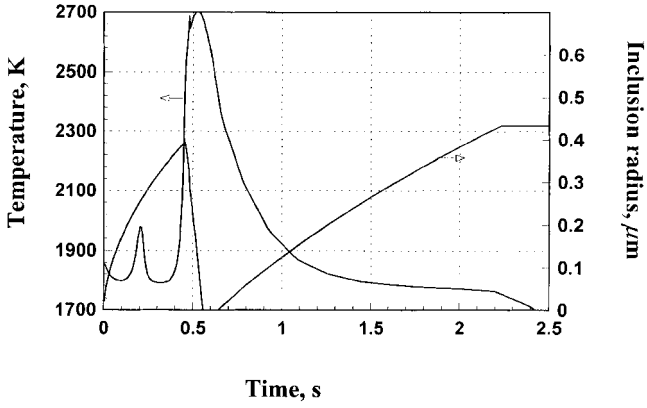

Fig. 9—An example of extensive dissolution of an Al_2O_3 inclusion with corresponding thermal excursions.

D. *Effect of Thermal Excursions on Inclusion Formation*

Two typical temperature-time plots and the corresponding inclusion radius–time plots are shown in Figures 9 and 10. Figure 9 shows an inclusion growth with extensive dissolution. Figure 10 shows an inclusion growth with limited dissolution. Figure 10 also shows that inclusion begins to dissolve at about 2240 K and grows again when the temperature falls below 2200 K. Its radius reaches about 0.46 μm before it is engulfed in the solidifying weld metal. From Figure 8, it is known that the majority of the inclusions are exposed to temperatures above 2240 K. Therefore, the effect of dissolution on the inclusion size distribution must be significant. Figure 3 indicates that the other oxides are much more unstable than Al_2O_3. Therefore, the dissolution of other oxides is expected to be more extensive than that of Al_2O_3. The computed equilibrium dissolution temperature of Al_2O_3 is 2245 K. Thermodynamically, the inclusion must grow once it is cooled below 2245 K. However, the maximum temperature for growth observed in the TTT diagram in Figure 1 is 45 K lower than 2245 K. This apparent difference is related to the amount of undercooling needed to nucleate certain inclusions to satisfy the condition for $\zeta = 0.01$.

Figure 11(a) shows the size distribution of the Al_2O_3 inclusion. It is observed that most inclusions are smaller than 1 μm. The coarsening of inclusions is aided by the long residence times. The size distributions of inclusions are presented in Figure 11(b) as a plot of percentage *vs* radius of inclusions. The computed size distribution is in good agreement with the measured values. Before comparison, the experimental two-dimensional measurements are converted to three-dimensional diameters, assuming Fullman theory[24] for a polydispersed system of spheres. The main difference between the experimental and the computed results is that the measured values show fewer small inclusions in the size range from 0 to 0.16 μm. One possible reason for this discrepancy may be the inability to detect small inclusions by optical microscopy. Another reason could be related to the inherent assumption in the model that inclusions smaller than the critical nucleation size still exist and that they continue to grow without disappearing. The effect of collision and coalescence on inclusion size distribution was also considered. The calculated results of number density with and without considering the collision of inclusions are shown in Figures 12(b) and (a), respectively. It can be observed that the size distribution moves to a higher size, while the distribution curve of the number density becomes broader and the maximum number density becomes lower when the collision model is taken into account.

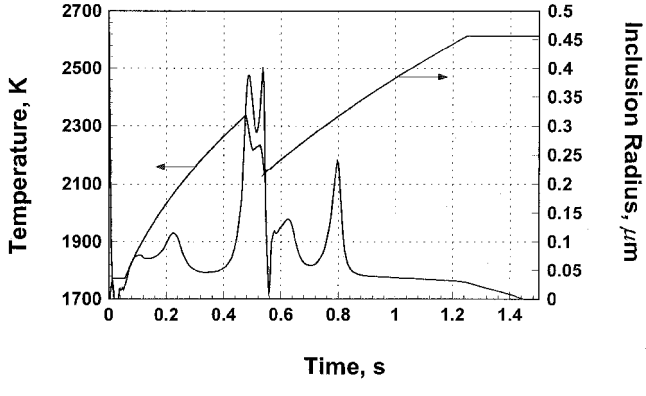

Fig. 10—An example of Al_2O_3 inclusion growth with limited dissolution with corresponding thermal excursions.

In the past, the mechanism of inclusion growth has been investigated by examining how the inclusion radius changes with time. For example, if the inclusions grow by Ostwald ripening[25] at the liquidus temperature and the diffusion of oxygen is considered, the expression of final mean inclusion diameter ($\overline{d}$) as a function of t is given by the Wagner equation,[26]

$$\overline{d}^3 = \overline{d}_{\text{ini}}^3 + \frac{64\sigma D_O C_O V_m}{9\,RT}\, t \approx Ct \qquad [15]$$

where D_O is the diffusivity of oxygen, C_O is the bulk oxygen concentration, $\overline{d}_{\text{ini}}$ is the initial mean diameter of inclusions, V_m is the molar volume of the oxide, σ is the oxide-steel interfacial energy, R is the gas constant, T is the temperature, C is a proportionality constant, and t is the growth time of each inclusion. In our work, t is equal to the residence time of the inclusions in the liquid region. The calculated mean size from the Wagner equation and the sizes of several inclusions as a function of $t^{1/3}$ are shown in Figure 13. It is interesting to observe that the calculated results show good agreement with the Wagner equation, although the growth and dissolution of the inclusions were calculated by assuming diffusion control, considering temperature gyrations experienced by the inclusions. These results do not rule out the possibility of Ostwald ripening. However, it shows that examining the mechanism of inclusion growth based on how the inclusion size varies with time can lead to completely misleading conclusions.

IV. CONCLUSIONS

1. The TTT diagrams of growth and dissolution of oxide inclusions show that Al_2O_3 is the main oxide inclusion for the steel composition and welding parameters considered in this work.
2. The calculations show that most inclusions experience both growth and dissolution during their residence in the weld pool.
3. Trends of computed results agree with experimentally observed inclusion size distributions and indicate that

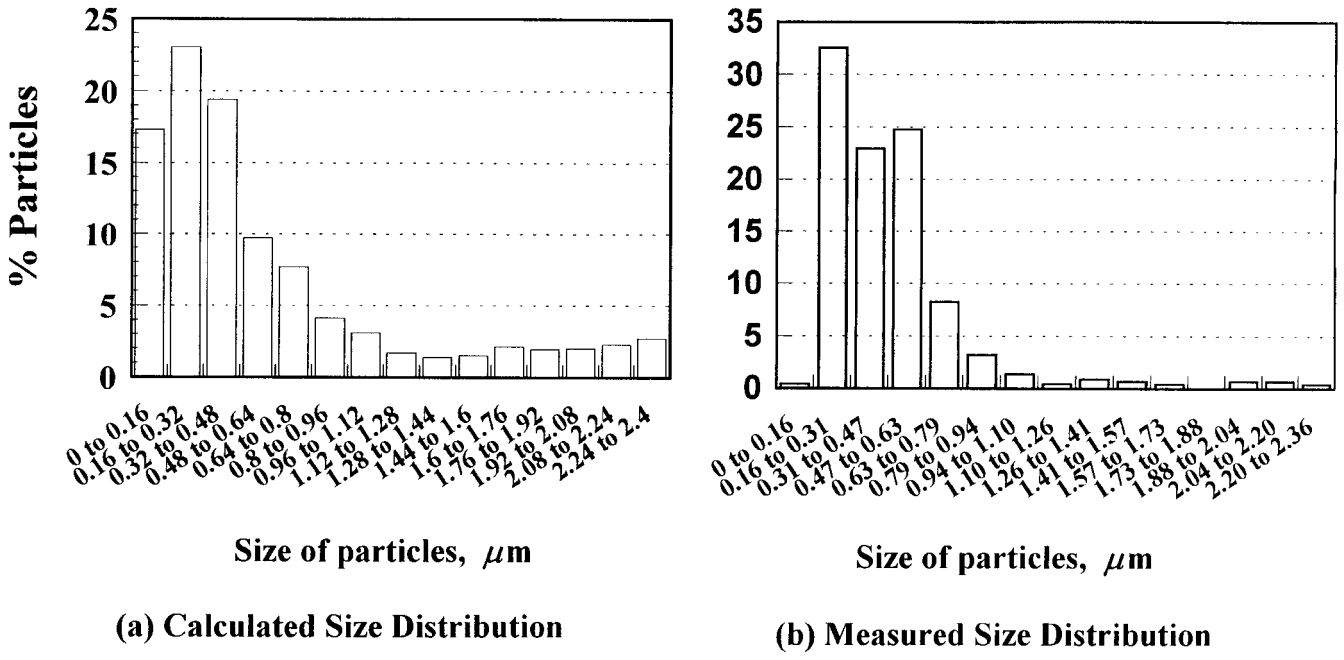

Fig. 11—Comparison of (*a*) the calculated and (*b*) the measured size distributions, of Al_2O_3 inclusions in the low alloy steel weld pool.

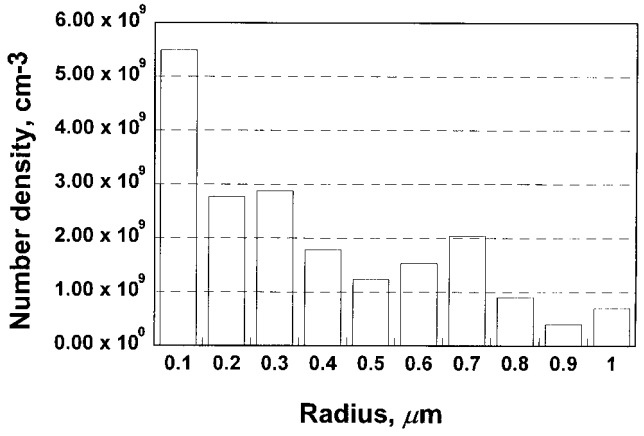

(*a*)

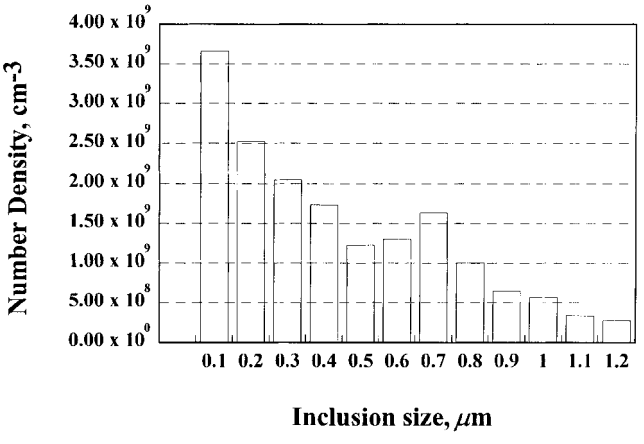

(*b*)

Fig. 12—(*a*) Calculated number density of inclusion size considering homogeneous nucleation rate without considering collision. (*b*) Modified number density of inclusion size considering collision model.

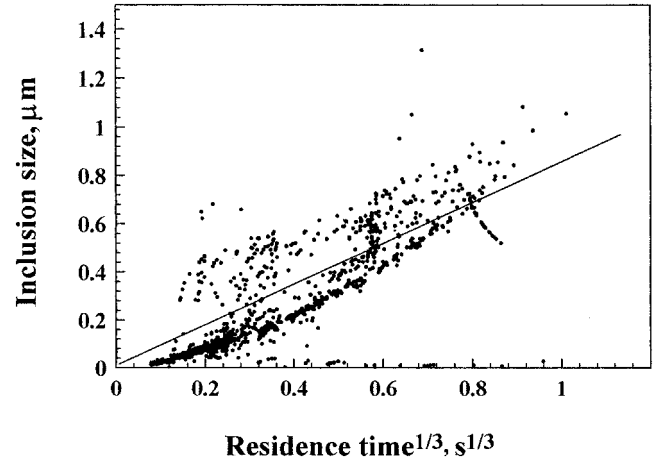

Fig. 13—Comparison between calculated results of inclusion sizes from this work and the Wagner equation.

inclusion growth can be understood from the fundamentals of transport phenomena and kinetics.

4. Considering diffusion-controlled growth and dissolution of inclusions, the increase in inclusion size with residence time exhibited a pattern characteristic of the Wagner equation, derived considering Ostwald ripening. Thus, special care should be exercised to evaluate the inclusion growth mechanism from the experimentally measured inclusion size as a function of time.

APPENDIX Derivation of collision model

The number of collisions per unit volume per unit time between two inclusions of size r_1 and r_2 is given by

$$N(r_1, r_2) = W(r_1, r_2)n(r_1)n(r_2) \quad [1]$$

where $n(r_1)$ and $n(r_2)$ are the number density of r_1 and r_2

inclusions (*i.e.*, the inclusion numbers per unit volume) and $W(r_1, r_2)$ is the collision volume, which is the probability of collision between two inclusions of size r_1 and r_2 within a unit time. For gradient collisions, W is given by

$$W = \frac{4}{3}(r_1 + r_2)^3 \text{ grad } v \qquad [2]$$

In our calculation, we assumed a constant gradient of v (grad v), which is equal to 0.03. This value is estimated using Eq. [11] in Reference 16. When two inclusions with a radius of r_1 and r_2 collide, a new inclusion of size $r = \sqrt[3]{r_1^3 + r_2^3}$ forms to keep the volume constant. Therefore, there is a decrease at the number densities of inclusions with radii of r_1 and r_2, while there is an increase at the number density of inclusion of radius r.

If we consider the collisions of $n(r)$ inclusions of size r and of $n(r_3)$ inclusions of size r_3, the collision number between the inclusions, which range in size from r_3 to $r_3 + dr_3$, and the inclusions of size r within a unit time (*i.e.*, annihilation rate of $n(r)$ due to size range of dr_3) is $W(r, r_3)\ n(r)n(r_3)dr_3$. If we integrate the variable r_3, the total annihilation rate of r inclusions for the whole size range is given by

$$\frac{dn(r)}{dt} = -\int_0^{r_{max}} n(r)n(r_3)W(r, r_3)\, dr_3 \qquad [3]$$

Suppose we have an inclusion with the radius of r_1 colliding with another inclusion to form a new inclusion. To get an inclusion of the radius between r and $r + dr$, the other inclusion's radius must be in the range from $\sqrt[3]{(r + dr)^3 - r_1^3}$ to $\sqrt[3]{r^3 - r_1^3}$. When we substitute r with $r = \sqrt[3]{r_1^3 + r_2^3}$ and do the series expansion, this size range can be written to be from $r_2 + (r/r_2)^2\, dr$ to r_2. When we have $n(r_1)$ inclusions of size r_1, from the same discussion as in the proceeding text, and take dr_2 to be $(r/r_2)^2\, dr$, the generation rate of an inclusion of size r is given by

$$W(r_1, r_2)n(r_1)\, n(r_2)\left(\frac{r}{r_2}\right)^2 dr \qquad [4]$$

Inclusions of all sizes, from $r_1 = 0$ to $r_1 = r$, may contribute to form new inclusions of a radius of r, so we need to integrate r_1 from 0 to r. This integration includes every inclusion twice, once as r_1 and once as r_2, so the result must be divided by 2. We then get the generation effect on the change rate of number density of size r.

$$\frac{dn(r)}{dt} = \frac{1}{2}\int_0^r n(r_1)n(r_2)\, W(r_1, r_2)\left(\frac{r}{r_2}\right)^2 dr_1, \qquad [5]$$

$$\text{with } r_2^3 = r^3 - r_1^3$$

When we consider the increasing and annihilation effect for the number density of size r, we can get the following change rate:

$$\frac{dn(r)}{dt} = \frac{1}{2}\int_0^r n(r_1)W(r_1, r_2)f(r_2)\left(\frac{r}{r_2}\right)^2 dr_1 - \int_0^{r_{max}} f(r_3)W(r, r_3)\, f(r)dr_3, \text{ with } r_2^3 = r^3 - r_1^3 \qquad [6]$$

ACKNOWLEDGMENTS

The present study was supported by the Division of Materials Sciences, Office of Basic Energy Sciences, the United States Department of Energy, under Grant No. DE-FG02-84ER45158 with Penn State and under Contract No. DE-*05-96OR22464 with Lockheed Martin Energy Research Corporation. The authors thank Messrs. W. Pitscheneder and Z. Yang for their interest in this research.

REFERENCES

1. D.J. Abson: *Welding World*, 1989, vol. 27, pp. 76-101.
2. R.H. Frost and D.L. Olson: *Intl. Trends in Welding Science and Technology*, S.A. David and J.M. Vitek, eds., ASM Intl., Ohio, 1992, pp. 213-22.
3. F.J. Barbaro, P. Krauklis, and K.E. Easterling: *Mater. Sci. Technol.*, 1989, vol. 5, pp. 1057-68.
4. A.O. Kluken and O. Grong: *Metall. Trans. A*, 1989, vol. 20A, pp. 1335-49.
5. S.A. Court and G. Pollard: *Metallography*, 1989, vol. 22, pp. 219-43.
6. O. Grong, A.O. Kluken, H.K. Hylund, A.L. Dons, and J. Hjelen: *Metall. Mater. Trans. A*, 1995, vol. 26A, pp. 525-34.
7. Y. Horii, K. Ichikawa, S. Ohkita, S. Funaki, and N. Yurioka: *Q. J. Jpn. Welding Soc.*, 1995, vol. 13, pp. 500-12.
8. K.C. Hsieh, S.S. Babu, J.M. Vitek, and S.A. David: *Mater. Sci. Eng.*, 1996, vol. A215, pp. 84-91.
9. S.S. Babu, S.A. David, J.M. Vitek, K. Mundra, and T. DebRoy: *Mater. Sci. Technol.*, 1995, vol. 11, pp. 186-99.
10. S.S. Babu, S.A. David, and T. DebRoy: *Sci. Technol. Welding Joining*, 1996, vol. 1, pp. 17-27.
11. T. Hong, W. Pitscheneder, and T. DebRoy: *Sci. Technol. Welding Joining*, 1997, vol. 2, pp. 1-9.
12. K. Mundra, T. DebRoy, and K.M. Kellkar: *Num. Heat Transfer*, 1996, Part A, vol. 29, pp. 115-29.
13. S. Kumar and S.C. Bhaduri: *Metall. Mater. Trans. B*, 1994, vo1. 25B, pp. 435-41.
14. M. Ushio and C.S. Wu: *Metall. Mater. Trans. B*, 1997, vol. 28B, pp. 509-16.
15. R.K. Iyengar and W.O. Philbrook: *Metall. Trans.*, 1972, vol. 3, pp. 1823-30.
16. U. Lindborg and K. Torssell: *Trans. TMS-AIME*, 1968, vol. 242, pp. 94-102.
17. S.V. Patankar: *Numerical Heat Transfer and Fluid Flow*, McGraw-Hill Book Company, New York, NY, 1980
18. G.K. Sigworth and J.F. Elliott: *Met. Sci.*, 1974, vol. 8, pp. 298-310
19. C. Zener: *J. Appl. Phys.*, 1949, vol. 20, pp. 950-52
20. J.W. Christian: *The Theory of Transformations in Metals and Alloy—Part I: Equilibrium and General Kinetic Theory*, 2nd ed., Pergamon Press, Oxford, United Kingdom, 1981.
21. M.J. Whelan: *Met. Sci. J.*, 1969, vol. 3, pp. 95-97
22. J.B. Scarborough: *Numerical Mathematical Analysis*, 6th ed., The Johns Hopkins Press, Baltimore, MD, 1966, pp. 320-24
23. W. Pitscheneder, R. Ebner, T. Hong, T. DebRoy, K. Mundra, and R. Benes: *Mathematical Modeling of Weld Phenomena 4,* H. Cerjak and H.K.D.H. Bhadeshia, The Institute of Materials, London, England, 1998, pp. 3-25.
24. R.L. Fullman: *Trans. AIME*, 1953, vol. 197, pp. 447-52
25. L. Ratke and W.K. Thieringer: *Acta Metall.*, 1985, vol. 33, pp. 1793-1802
26. C. Wagner: *Z. Elecktrochemie*, 1961, vol. 65, pp. 581-91